



# Carbon modification facilitates piezocatalytic H<sub>2</sub>O<sub>2</sub> production over BiOCl nanosheets: Correlation between piezoresponse and surface reaction

Yuanyi Zhou<sup>a,b,1</sup>, Haojie Dong<sup>b,1</sup>, Zhaofen Xu<sup>b</sup>, Qingbing Zha<sup>a</sup>, Mingshan Zhu<sup>a,b,\*</sup>,  
Yu Meng<sup>a,\*\*</sup>

<sup>a</sup> Nephrology Department & Guangdong Provincial Key Laboratory of Spine and Spinal Cord Reconstruction, The Fifth Affiliated Hospital of Jinan University (Heyuan Shenhe People's Hospital), Heyuan 517465, China

<sup>b</sup> School of Environment, Jinan University, Guangzhou 511443, China

## ARTICLE INFO

### Keywords:

Piezocatalysis  
H<sub>2</sub>O<sub>2</sub> production  
BiOCl  
Surface modification

## ABSTRACT

Piezocatalysis offers a facile approach for the production of H<sub>2</sub>O<sub>2</sub>, which is a green fuel and oxidant with broad application scenarios. Clarifying the role of various factors is critical to the rational design of the piezocatalytic system. Herein, carbon species are modified over BiOCl nanosheets, achieving a piezocatalytic H<sub>2</sub>O<sub>2</sub> production rate of 2110 μmol g<sup>-1</sup> h<sup>-1</sup> in pure water. Mechanistic studies reveal that although the modification weakens the piezoelectricity of BiOCl, the contribution of carbon species in raising the carrier density and serving as the O<sub>2</sub> activation sites promotes H<sub>2</sub>O<sub>2</sub> generation. As a result, the decline of piezoresponse is surmounted by the improvement in surface reaction, and the piezocatalytic activity of C-BiOCl outperforms the pristine BiOCl nanosheets. This work emphasizes that the surface active site is the bridge connecting piezoelectricity and catalytic efficiency, which puts forward an insightful strategy for the modularization of the piezocatalytic system.

## 1. Introduction

Hydrogen peroxide (H<sub>2</sub>O<sub>2</sub>) is a green fuel and oxidant with a high energy density (2.1 MJ kg<sup>-1</sup>), which has a wide range of application scenarios [1–3]. Onsite production of H<sub>2</sub>O<sub>2</sub> through renewable energy conversion is undoubtedly a promising approach that avoids the inconvenience of long-distance transportation. Among the reported solutions, piezocatalysis has drawn extensive attention. This technique represents a couple of piezoelectric effect and electrochemical reactions, converting easily available mechanical energies such as sounds, waves, and vibrations directly into chemical energies [4–10]. Without the restriction of time and location, piezocatalytic H<sub>2</sub>O<sub>2</sub> production displays great potential in energy conversion, environmental remediation as well as disease treatment [11–15].

To improve efficiency, many efforts have been devoted to regulating the response behavior of piezoelectrics under external mechanical stress [16–18]. Li et al. introduced epitaxial interphase strain into BaTiO<sub>3</sub> nanoparticles, resulting in a significant increase of the tetragonality,

piezoelectricity, and thus the overall water-splitting activity [19]. In the previous work, we also found that the piezocatalytic performance of Ba<sub>0.5</sub>Sr<sub>0.5</sub>TiO<sub>3</sub> was superior to SrTiO<sub>3</sub> because of the enhanced asymmetry in the perovskite nanoparticle by Ba substitution [20]. These reports emphasize the importance of piezoresponse, which decides the energy input in this system. For the subsequent catalytic reaction, the rational design of the active sites also deserves grave concerns. Regarding H<sub>2</sub>O<sub>2</sub> production specifically, the reactivity is highly dependent on the surface physicochemical properties of the piezoelectric, such as the capability of O<sub>2</sub> adsorption and activation [21,22]. Yet, how surface reaction correlates with piezoresponse remains to be explored.

Proceeding from the correlation, herein, bismuth oxychloride (BiOCl) was selected as a model piezocatalyst for the production of H<sub>2</sub>O<sub>2</sub>. The layered structure composed of [Cl–Bi–O–Bi–Cl] building blocks made it a competent candidate for piezocatalytic H<sub>2</sub>O<sub>2</sub> production in pure water [23–27]. With the commonly exposed (001) facets and spontaneous polarization along [001] direction, BiOCl nanosheets provide a suitable platform for O<sub>2</sub> reduction. In regard to the active sites,

\* Corresponding author at: Nephrology Department & Guangdong Provincial Key Laboratory of Spine and Spinal Cord Reconstruction, The Fifth Affiliated Hospital of Jinan University (Heyuan Shenhe People's Hospital), Heyuan 517465, China.

\*\* Corresponding author.

E-mail addresses: [zhumingshan@jnu.edu.cn](mailto:zhumingshan@jnu.edu.cn) (M. Zhu), [mengy@jnu.edu.cn](mailto:mengy@jnu.edu.cn) (Y. Meng).

<sup>1</sup> These authors contribute equally to this study.

carbon species with abundant surface oxygen-containing functional groups are preferred. The carbon atoms adjacent to several functional groups exhibit certain affinity towards two-electron  $O_2$  reduction [28–30]. In the present work, after the successful fabrication of carbon-modified BiOCl (C-BiOCl) nanosheets, the role of carbon species in both piezoresponse and  $H_2O_2$  generation was analyzed. On one hand, although carbon modification elevated the carrier density and regulated the conduction band minimum, the piezoelectricity of BiOCl was weakened, which went against the common practice of improving piezoresponse. On the other hand,  $O_2$  activation was facilitated with the introduction of surface active sites. It turned out that the promotion in  $O_2$  reduction made up for the negative impact on piezoelectricity decline, leading to an enhancement of the piezocatalytic  $H_2O_2$  generation efficiency over C-BiOCl ( $2110 \mu\text{mol g}^{-1} \text{h}^{-1}$ ) which was nearly twice to that of the pristine BiOCl nanosheets ( $1225 \mu\text{mol g}^{-1} \text{h}^{-1}$ ). This outcome was conducive to the modular design of the piezocatalytic system.

## 2. Experimental section

### 2.1. Materials

All the chemicals involved were of analytical grade, purchased from Sinopharm Chemical Reagent Co., Ltd., and used without further purification.

### 2.2. Preparation of BiOCl catalysts

Surface carbon-modified BiOCl (C-BiOCl) was synthesized by hydrothermal method and post-calcination. A typical process was to grind and mix 310 mg of  $\text{Bi}(\text{NO}_3)_3 \cdot 5\text{H}_2\text{O}$  and 25 mg of glucose in a mortar. The mixture was slowly added to 80 mL of deionized water under ultrasonic conditions. 48 mg of KCl was then added. After stirring for 30 min, the suspension was transferred to a 100 mL PTFE-lined stainless-steel autoclave, and heated at  $160^\circ\text{C}$  for 18 h. The obtained samples were collected, washed 3 times with deionized water and ethanol, dried in an oven, and then calcined in the muffle furnace at  $450^\circ\text{C}$  for 4 h at a heating rate of  $5^\circ\text{C min}^{-1}$  to be used. Pristine BiOCl was synthesized through the same procedure without the addition of glucose. The reference carbon material sample was synthesized through the same procedure without the addition of  $\text{Bi}(\text{NO}_3)_3 \cdot 5\text{H}_2\text{O}$ .

### 2.3. Preparation of deactivated C-BiOCl catalysts

Phenyl-hydrazine (PH), benzoic anhydride (BA), and 2-bromo-1-phenylethanone (BrPE) were employed as high-specificity deactivating agents to react with C=O, C–OH, and COOH functional groups on C-BiOCl. For the deactivation of C=O groups, 200 mg of PH was dissolved in 10 mL of  $\text{CHCl}_3$  with the addition of 10  $\mu\text{L}$  of hydrochloric acid (38 %). 50 mg of C-BiOCl nanosheets were then dispersed in the solution above and stirred for 72 h at room temperature and under  $N_2$  protection. The precipitate was washed with ethanol several times to remove the weakly adsorbed PH molecules, dried in an oven, and denoted as C-BiOCl-PH to be tested. For the deactivation of C–OH groups, the procedure was similar except the solution was 10 mL of  $\text{CHCl}_3$  dissolving 1 g of BA, the suspension was stirred for 24 h at  $60^\circ\text{C}$ , and the sample was denoted as C-BiOCl-BA. For the deactivation of COOH groups, the procedure was also similar except the solution was 10 mL of  $\text{CHCl}_3$  dissolving 400 mg of BrPE, the suspension was stirred for 5 h in the dark, and the sample was denoted as C-BiOCl-BrPE.

### 2.4. Characterization

X-ray diffraction (XRD) patterns were collected on a D8 ADVANCE X-ray spectrometer (Bruker, Germany). Scanning electron microscopy (SEM) and energy-dispersive X-ray (EDX) spectroscopy were conducted

on a JSM-6330F scanning electron microscope (JOEL, Japan). Transmission electron microscopy (TEM) images were recorded on a JEM-2100F transmission electron microscope (JOEL, Japan). Fourier-transform infrared (FTIR) spectroscopy was recorded on an IRTracer-100 spectrometer (Shimadzu, Japan). Raman spectra were measured by a Nicolet NXR 9650 Raman microscope (Thermo-Fisher, USA). X-ray photoelectron spectroscopy (XPS) measurements were performed on an ESCALAB 250 photoelectron spectrometer (Thermo-VG Scientific, USA). For the analysis of the XPS results, *Avantage* software was used. C–C signal at 284.8 eV in the C 1s XPS spectrum was used as a charge correction reference. The FWHM is set in a range of 0.8–1.8 eV and constrained in the same component. Gaussian-Lorentzian line shape GL (30) curves were used for curve fitting. The core-level energy splitting and core-level area ratios were automatically set according to the software database. Specifically, for the analysis of Cl 2p spectra, the core-level energy splitting was around 1.60 eV and the core-level area ratio of  $2p_{3/2}$  to  $2p_{1/2}$  was 2:1. For the analysis of Bi 4f spectra, the core-level energy splitting was around 5.30 eV and the core-level area ratio of  $4f_{7/2}$  to  $4f_{5/2}$  was 4:3. The assignment of fitting results was determined by the NIST XPS database (<https://srdata.nist.gov/xps>) and the reported articles. UV–visible-near infrared diffuse reflectance spectroscopy (DRS) was conducted on a V-770 spectrometer (JASCO, UK). Atomic force microscopy (AFM) and piezoresponse force microscopy (PFM) were measured by a Cypher Asylum Research microscope (USA). Oxygen temperature-programmed desorption ( $O_2$ -TPD) was performed on a Mettler TGA/DSC3 + chemisorption analyzer (Switzerland). Typically, the sample was pretreated under Ar atmosphere at  $400^\circ\text{C}$  for 2 h. When the system cooled down to room temperature, the atmosphere was switched to  $O_2$  and maintained for 2 h. Then the system was again switched to Ar atmosphere and heated to  $600^\circ\text{C}$  at a rate of  $10^\circ\text{C min}^{-1}$ . The signal of  $O_2$  desorption was monitored by a TCD detector. All the rate of gas flow was set to  $100 \text{ mL min}^{-1}$ . Thermogravimetric analysis was carried out on a Mettler TGA/DSC (Switzerland) and a STA2500 Regulus (NETZSCH, German) thermal analyzer in flowing  $N_2$  at a heating rate of  $10^\circ\text{C min}^{-1}$  (Fig. S12). The TG results indicated negligible weight loss under  $400^\circ\text{C}$ . Considering the post-calcination at  $450^\circ\text{C}$  during the fabrication, the samples would remain stable in the desorption pretreatment procedure of  $O_2$ -TPD tests.

### 2.5. Electrochemical analyses

Electrochemical characterization was conducted on a CHI 760E electrochemical workstation (Chenhua, China) with a conventional three-electrode cell system: a glassy carbon electrode deposited with catalysts as the working electrode, Pt wire as the counter electrode, Ag/AgCl as the reference electrode. Mott-Schottky curves, electrochemical impedance spectra (EIS), and transient current response were collected in 0.5 M  $\text{Na}_2\text{SO}_4$  solution. It should be noted that the catalysts were dispersed in the electrolyte solution during the test of the transient current response. The carrier density of the sample derived from the Mott-Schottky curve was calculated by the following formula [31].

$$N_D = \left( \frac{2}{\epsilon \epsilon_0 q} \right) \left( \frac{dE}{d(1/C^2)} \right) = \left( \frac{2}{\epsilon \epsilon_0 q} \right) \left( \frac{1}{\text{slope}} \right)$$

where  $N_D$  was the carrier density,  $\epsilon$  was the dielectric constant of BiOCl (i.e. 3.5) [32],  $\epsilon_0$  was the permittivity of the vacuum, and  $q$  was the electronic charge unit.

### 2.6. Piezocatalytic $H_2O_2$ production

All the procedure was consistent if not specified. Generally, an open 250 mL beaker was used as the reactor, immobilizing above the ultrasonic transducer in a KS-2200DB ultrasonic cleaner (Kunshan Jielimei, China). The power and frequency of the equipment was 100 W and 40 kHz, respectively. The temperature of the water bath was controlled

at room temperature by running tap water and the water level was equal to the liquid level in the beaker. The system was stirred at 400 rpm by a JJ-1B-200W agitating machine (Xinrui, China) during the whole test (Fig. S13). 20 mg of BiOCl catalyst was dispersed into 100 mL deionized water under stirring. Then the ultrasonic vibration was exerted on the suspension. The concentration of  $\text{H}_2\text{O}_2$  was determined by the iodide spectrophotometric method. For details, 1 mL filtrate from the suspension was added into a solution containing 4 mL of 0.1 M potassium iodide and 0.1 mL of 0.01 M ammonium molybdate. The absorbance at 350 nm was detected by a V-770 spectrometer (JASCO, UK) after 15 min standing. To be noted, considering that the carbon content over C-BiOCl was quite limited, the mixture of carbon materials and BiOCl nanosheets contained 1 mg reference carbon material and 19 mg BiOCl nanosheets in the control experiments. In the experiments under different atmospheres, atmosphere control was achieved by continuously blowing a flowing specified gas above the suspension. In the cycling tests, the sample after each cycle was centrifuged, washed with deionized water several times, dried in an oven at 60 °C overnight, and then subjected to the next cycle.

### 2.7. Electron spin resonance analyses

Electron spin resonance (ESR) spectra were recorded on an EMXnano spectrometer (Bruker, USA) using 5,5-dimethyl-1-pyrroline N-oxide (DMPO) as the spin-trapping agent. For the in situ ESR analyses, 5 mg of catalyst was dispersed in 5 mL of dimethyl sulfoxide with 50  $\mu\text{L}$  of DMPO added. The system was saturated and bubbled by air. A peristaltic pump was equipped for sample injection into the test chamber of the EMXnano spectrometer. Data processing was performed through the equipped *Xenon* software. The *SpinFit* module in the software was a spin trap fitting routine that disentangled the various spin adducts and calculated the double integral for each individual component. Combined with the spin counting module the double integral was converted into the number of spins for each species. When the contribution of the signal was higher than 70 %, the corresponding spin adduct was considered to be dominant. Standard ESR spectra of  $\text{DMPO-O}_2^{\cdot-}$  and  $\text{DMPO-HO}_2^{\cdot}$  adducts in the software database are shown in Fig. S14.

## 3. Results and discussion

The structure and morphology of BiOCl catalysts were first characterized. The XRD patterns of both pristine and carbon-modified BiOCl (Fig. S1) were well-indexed to the tetragonal phase structure (PDF#06-0249), and no other impurity peaks were found. The crystallinity of BiOCl was reduced after carbon modification. The intensity ratios of the (002) and (200) peaks were 1.75 and 0.56 for BiOCl and C-BiOCl, respectively, indicating that the facet exposure might change after the decoration of carbon species. In the SEM images (Fig. 1a and b), the as-prepared BiOCl catalysts displayed nanosheet-like morphology. The predominant morphology of the BiOCl nanosheet changed from a square shape to an irregular shape. EDX mapping (Fig. S2) suggested the uniform distribution of carbon elements upon the surface of BiOCl nanosheets. High-resolution TEM and selected area electron diffraction results (Fig. 1c–f) indicated that carbon modification did not change the growth orientation of BiOCl catalysts, and the exposed crystal planes were still {001} and {110}. AFM tests (Fig. S3) also revealed the thickness of  $\sim 100$  and  $\sim 50$  nm for BiOCl and C-BiOCl nanosheets correspondingly. The variation of crystallinity and morphology induced by carbon modification might affect the piezocatalytic performance.

Evolution brought by the addition of glucose precursor was then studied. In the FTIR spectra (Fig. 2a), an extra mode at around  $1060\text{ cm}^{-1}$  corresponding to C–O vibration was detected over C-BiOCl. [33,34] Meanwhile, as shown in the Raman spectra (Fig. 2b), three characteristic peaks of BiOCl at  $68.4$ ,  $152.6$ , and  $208.6\text{ cm}^{-1}$  were observed, which were assigned to the external  $A_{1g}$ , internal  $A_{1g}$ , and internal  $E_g$  vibration modes of Bi–Cl bond. Moreover, the spectrum of C-BiOCl displayed an additional vibration signal at  $1200\text{--}1700\text{ cm}^{-1}$ , which could be classified as surface carbon species. [35] The D band at  $1343\text{ cm}^{-1}$  and G band at  $1580\text{ cm}^{-1}$  could be distinguished from the data (Fig. S4) with an intensity ratio ( $I_D/I_G$ ) of 0.49, implying that there were defects in the surface-developed carbon species. XPS characterization was also conducted to investigate the carbon species on BiOCl. Element analyses from the XPS results (Table S1) indicated a higher surface carbon content for C-BiOCl than that for BiOCl. The C 1s XPS spectrum of C-BiOCl (Fig. 2c) could be deconvoluted into three peaks at 284.8, 286.5, and 288.6 eV, corresponding to C–C, C–O, and C=O bond, respectively. [36,37] This result agreed with the FTIR and Raman spectra above and also implied that there were abundant oxygen-containing

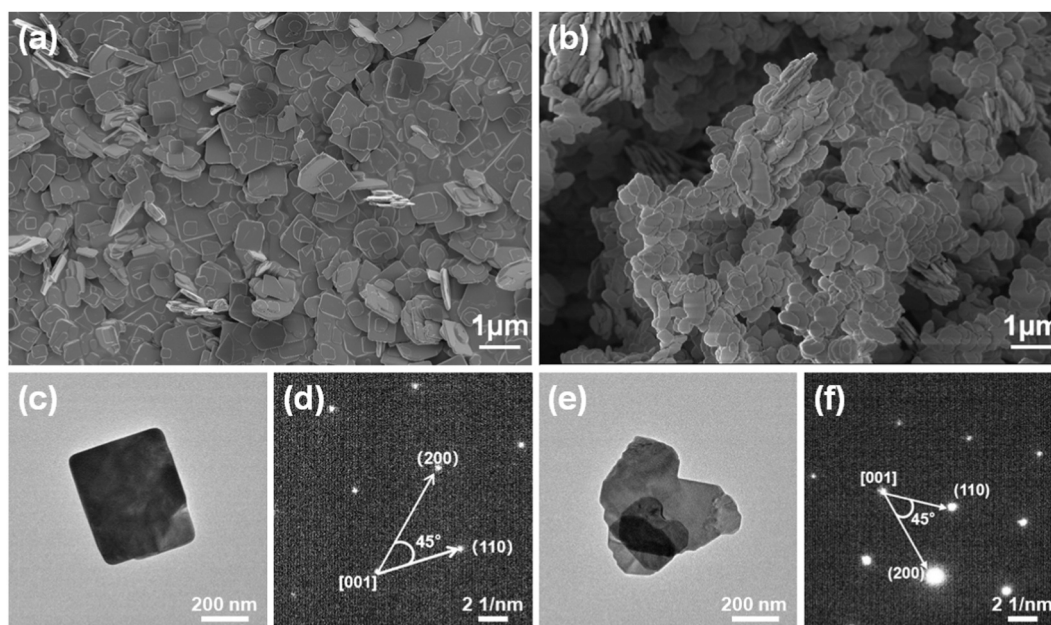


Fig. 1. SEM images of BiOCl (a) and C-BiOCl (b); High-resolution TEM and selected area electron diffraction images of BiOCl (c, d) and C-BiOCl (e, f).



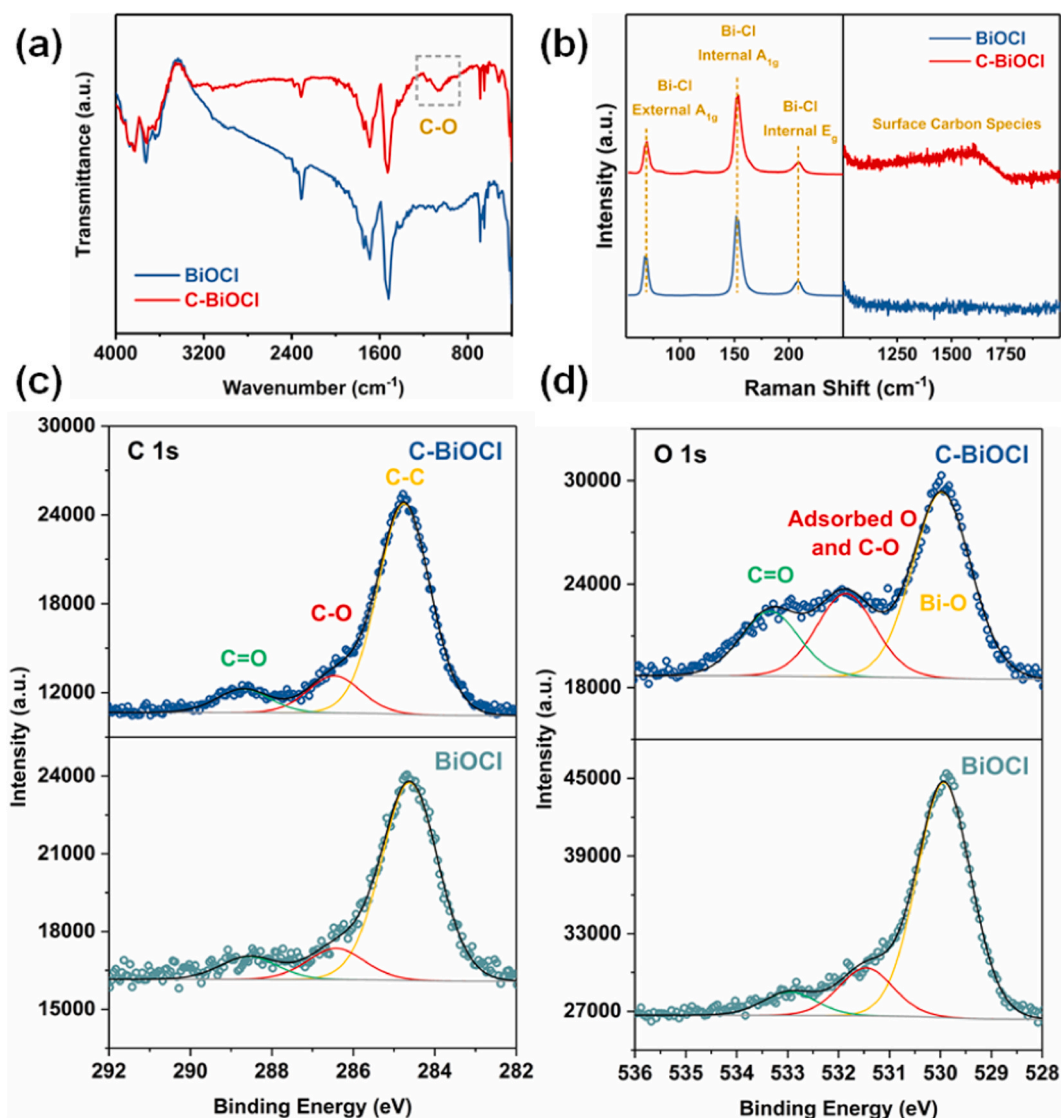


Fig. 2. (a) FTIR spectra, (b) Raman spectra, (c) C 1s XPS spectra, and (d) O 1s XPS spectra of BiOCl and C-BiOCl.

functional groups attached to the surface carbon species.[38,39] In the O 1s XPS spectrum of C-BiOCl (Fig. 2d), the signal could be fitted by three peaks at the binding energy of 530.0, 531.8, and 533.1 eV. The peak at 530.0 eV was characteristic of the Bi–O bond in BiOCl, while the signal at 531.8 eV was contributed by adsorbed oxygen species at the vacancy sites and surface C–O groups. The peak at 533.1 eV could be assigned to C=O groups on the surface [40]. The Bi 4f XPS spectra of the samples (Fig. S5) were assigned to the  $4f_{5/2}$  and  $4f_{7/2}$  orbitals of  $\text{Bi}^{3+}$  at 164.6 and 159.3 eV. No signal was found for the Bi species with a lower valence state, excluding the existence of  $\text{Bi}^0$  species. The Cl 2p XPS spectra could be identified as  $2p_{1/2}$  and  $2p_{3/2}$  orbitals of chlorine ions. Therefore, carbon species with abundant oxygen-containing functional groups were successfully decorated on BiOCl nanosheets.

The piezocatalytic performance of C-BiOCl nanosheets was subsequently evaluated. In the control experiments (Fig. 3a), the sonochemical event without the introduction of catalysts would lead to an  $\text{H}_2\text{O}_2$  production rate of  $4.9 \mu\text{mol h}^{-1}$ .  $\text{H}_2\text{O}_2$  production in the blank experiment was ascribed to the combination of  $\text{HO}^\bullet$ , which originated from the breakage of the H–O bond in  $\text{H}_2\text{O}$  molecules by the cavitation effect. Without the application of ultrasonic vibration, the concentration of  $\text{H}_2\text{O}_2$  was ignorable. The reference carbon species synthesized without the addition of the bismuth source was also tested but  $\text{H}_2\text{O}_2$  generation was negligible. The mixture of carbon materials and BiOCl nanosheets

displayed an  $\text{H}_2\text{O}_2$  production rate similar to BiOCl nanosheets alone. Without the introduction of any sacrificial agent, piezocatalytic  $\text{H}_2\text{O}_2$  production over the BiOCl catalysts was achieved. Fig. 3b revealed that the variation of glucose amount (0, 5, 10, 25, and 75 mg) led to a volcanic trend of  $\text{H}_2\text{O}_2$  production rate. The optimum reached  $2110 \mu\text{mol g}^{-1} \text{h}^{-1}$ , which was nearly twice that of the unmodified BiOCl ( $1225 \mu\text{mol g}^{-1} \text{h}^{-1}$ ), suggesting that the modification of carbon improved the piezocatalytic activity. The piezocatalytic  $\text{H}_2\text{O}_2$  generation efficiency remained above 90 % in five cycles (Fig. 3c). After cycling tests, The XRD pattern of the used C-BiOCl (Fig. S6) changed slightly compared to the fresh one. No obvious change occurred in the SEM images (Fig. S7). XPS analysis was also performed to check the surface microstructure (Fig. S8). The contents of C=O and C–O signals in the C 1s XPS spectra also displayed little variation. Moreover, long-term piezocatalytic  $\text{H}_2\text{O}_2$  production in pure water over C-BiOCl (Fig. 3d) achieved a concentration of  $11.53 \text{ mmol L}^{-1}$  after ultrasonication for 24 h. These results demonstrated acceptable stability, repeatability, and durability.

To elucidate the mechanism, p-benzoquinone (BQ) and tert-butyl alcohol (TBA) were applied to eliminate superoxide and hydroxyl radicals in the system. As shown in Fig. 4a and b, when the superoxide radicals were inhibited, the piezocatalytic  $\text{H}_2\text{O}_2$  production rate was cut by 70–90 % with the increase of BQ concentration, whereas the decline

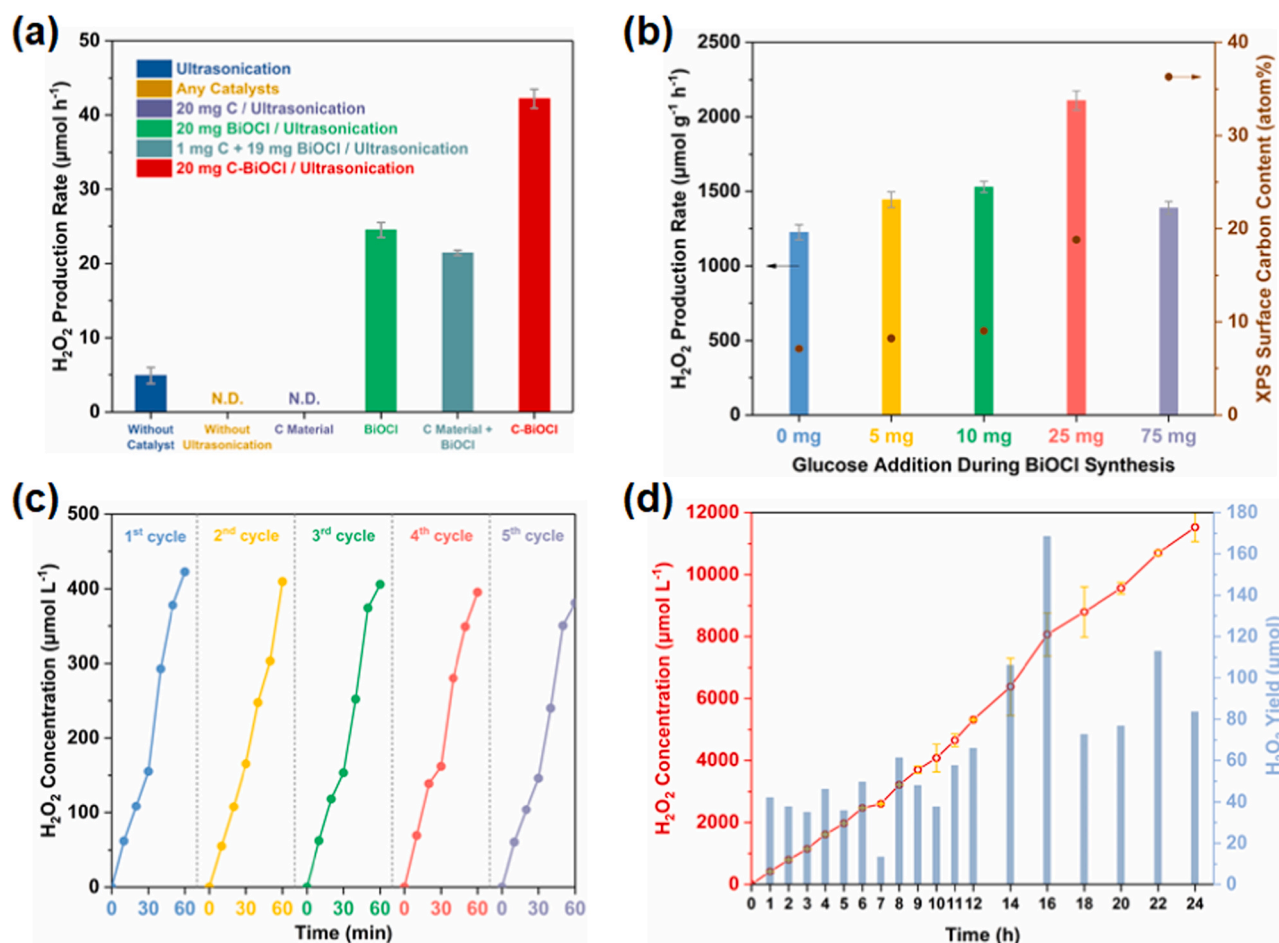


Fig. 3. (a) Control experiments of piezocatalytic  $\text{H}_2\text{O}_2$  production (None detected was denoted as N.D.). (b) Effect of glucose amount on the piezocatalytic  $\text{H}_2\text{O}_2$  production rate over BiOCl; (c) Cycling tests of piezocatalytic  $\text{H}_2\text{O}_2$  generation over C-BiOCl; (d) Long-term piezocatalytic  $\text{H}_2\text{O}_2$  production over C-BiOCl.

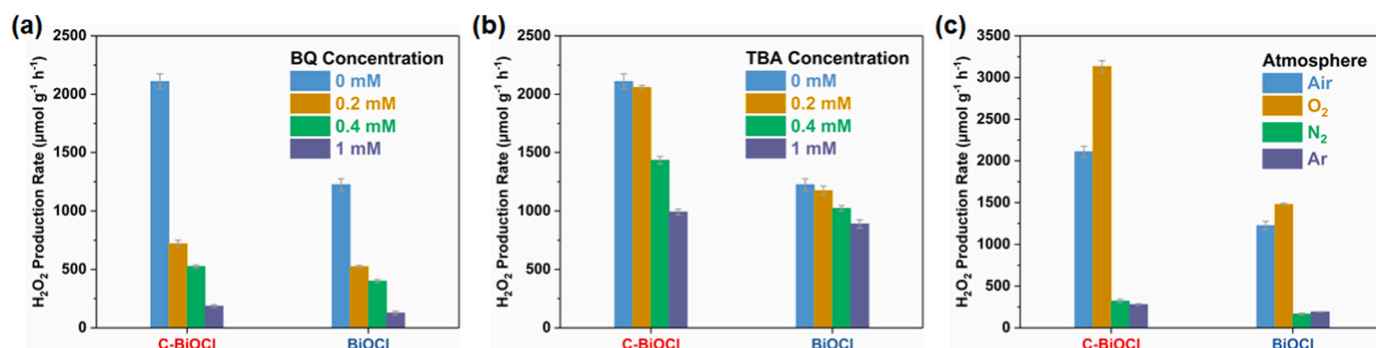


Fig. 4. (a) Superoxide radical-quenching tests over C-BiOCl and BiOCl; (b) Hydroxyl radical-quenching tests over C-BiOCl and BiOCl; (c) Piezocatalytic  $\text{H}_2\text{O}_2$  generation over C-BiOCl and BiOCl under different atmospheres.

from hydroxyl radical suppression was 10–60 %. Besides, when the atmosphere was switched to  $\text{N}_2$  or Ar, the generation of  $\text{H}_2\text{O}_2$  slowed down (Fig. 4c). The introduction of  $\text{O}_2$  further raised the  $\text{H}_2\text{O}_2$  production rate to 3134 and 1479  $\mu\text{mol g}^{-1} \text{h}^{-1}$  for C-BiOCl and BiOCl respectively. In comparison with the performance in air, C-BiOCl displayed a more noticeable improvement than that of BiOCl, providing another evidence that the modification of carbon species facilitated  $\text{O}_2$  reduction. Hence,  $\text{O}_2$  reduction was the predominant route in this process, and the efficiency was considerable (Fig. 5 and Table S2).

The improvement of piezocatalytic activity by carbon modification inspired the analyses of the immanent cause. The piezoelectric

properties of BiOCl and C-BiOCl were measured by PFM. As shown in Fig. 6a and b, both the typical  $\sim 180^\circ$  phase-voltage hysteresis loops and the amplitude-voltage butterfly-shaped curves were observed, confirming the intrinsic piezoelectricity of the catalysts. Notably, after carbon modification, the maximum amplitude of BiOCl decreased from  $\sim 17$  to  $\sim 4$  nm after carbon modification, which suggested a weakened piezoelectricity of C-BiOCl. The slopes derived from the butterfly-shaped curves were  $\sim 6.5$  and  $\sim 1.5$   $\text{nm V}^{-1}$  for BiOCl and C-BiOCl, respectively. It might reflect the variation trend of the piezoelectric  $d_{33}$  coefficient.

Band structure alignments assessed from the Mott-Schottky plots

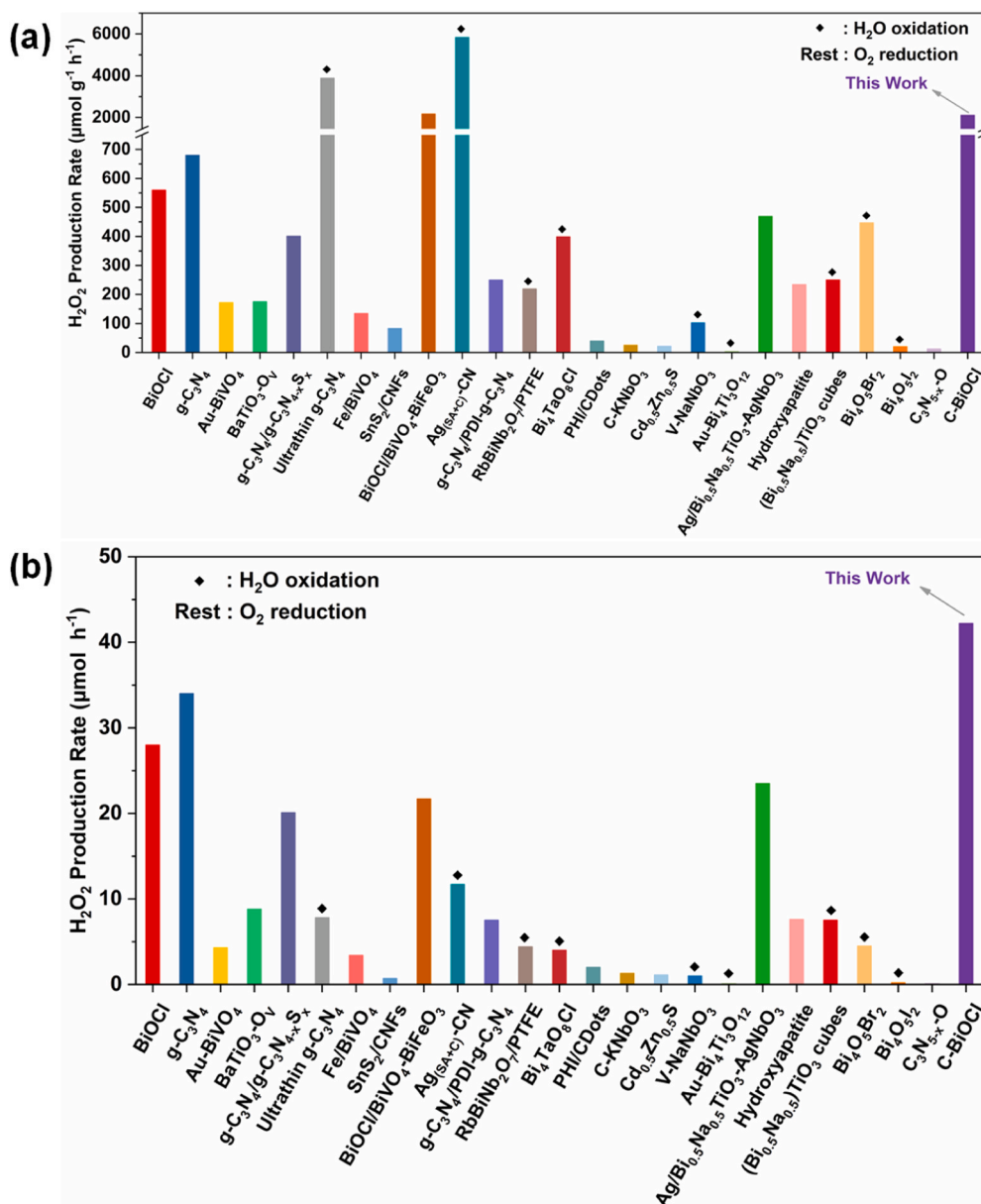


Fig. 5. Progress of piezocatalytic H<sub>2</sub>O<sub>2</sub> production in pure water by μmol g<sup>-1</sup> h<sup>-1</sup> (a) and μmol h<sup>-1</sup> (b).

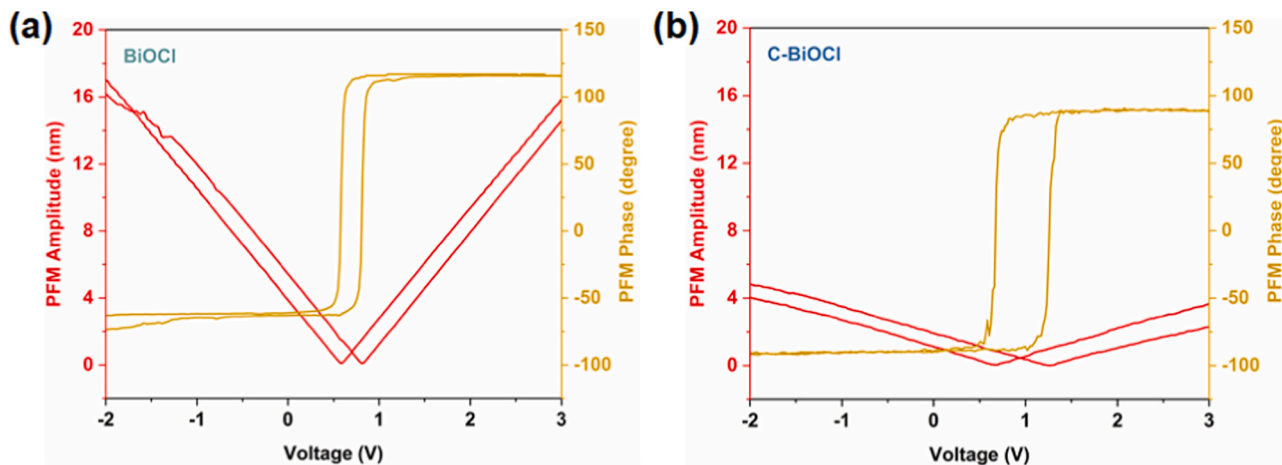


Fig. 6. Butterfly-shaped amplitude curve and hysteresis loop of BiOCl (a) and C-BiOCl (b).

(Fig. S9) and DRS spectra (Fig. S10) were presented in Fig. 7a. Without the application of mechanical stress, the reduction of  $O_2$  molecule (gaseous or aqueous) over BiOCl was thermodynamically unfavorable, whereas the reduction of aqueous  $O_2$  to  $HO_2^\bullet$  over C-BiOCl became possible. Under ultrasonic vibration, the piezoelectric effect would tilt the band structure alignments and compensate for the reaction barrier, thus triggering the thermodynamically infeasible processes. The conduction band minimum of BiOCl became more negative after carbon decoration, leading to a stronger driving force for the catalytic reduction. Free carriers were involved in both piezoresponse and surface reactions. Part of the free carriers in the piezocatalyst would be attracted and reside around the induced piezoelectric charges, thereby screening the piezopotential. Another part would migrate and be engaged in the surface reactions. A suitable concentration of free carriers promoted the surface reaction without greatly attenuating the piezopotential, which was beneficial to piezocatalysis. The carrier density of pristine BiOCl was also estimated. The introduction of surface carbon species elevated the carrier density of BiOCl to  $8.2 \times 10^{19} \text{ cm}^{-3}$ , which was roughly 8 times higher than that of the pristine BiOCl ( $9.6 \times 10^{18} \text{ cm}^{-3}$ ). The increased carrier concentration strengthened the internal screening effect while weakening the external one [41–44]. Accordingly, more free carriers in C-BiOCl would migrate and participate in the surface reaction driven by the piezopotential. Furthermore, in the electrochemical impedance spectra (Fig. 7b), a plot with a smaller radius was collected over C-BiOCl, implying faster charge transfer dynamics [45]. Thus, on one hand, the modification of carbon species led to the decline of piezoelectricity, which would weaken the piezoresponse under ultrasonic vibration, on the other hand, the band structure of C-BiOCl was regulated and the carrier density was raised, which would be beneficial to the catalysis. These characterizations also explained the volcano-type trend in piezocatalytic performance with an increasing amount of surface carbon species. Decoration of excessive carbon species would undermine the piezoresponse so that the driving force of catalytic reaction was diminished.

To probe  $O_2$  activation, the temperature-programmed desorption technique was applied. In the  $O_2$ -TPD spectra (Fig. 8a), a signal around  $270^\circ\text{C}$  was detected over the samples relating to the desorption of the chemisorbed  $O_2$  molecules, of which C-BiOCl was more intense than the pristine BiOCl. The amount of desorbed  $O_2$  upon BiOCl and C-BiOCl nanosheets was 0.667 and  $0.983 \text{ cm}^3 \text{ g}^{-1}$  respectively. This difference indicated that the carbon species might serve as the active center towards  $O_2$ . Transient current response under  $O_2$  atmosphere (Fig. 8b) provided another evidence that  $O_2$  activation over BiOCl was promoted after carbon modification. Besides, the performance of C-BiOCl after poisoning the surface C=O, C-OH, and COOH functional groups was also conducted (Fig. S11). The deactivation of C=O and COOH groups

barely affected the piezocatalytic performance, whereas the poisoning of C-OH groups suppressed the  $H_2O_2$  production rate to be close to the unmodified BiOCl, suggesting that the C-OH functional groups might be responsible for  $O_2$  activation.

As one of the critical intermediates in  $O_2$  reduction, the generation of superoxide radicals was also measured. Again, as shown in Fig. 9a, a more intense signal ascribed to the DMPO- $HO_2^\bullet$  adduct was received in the presence of C-BiOCl than that of BiOCl, suggesting that more  $O_2$  molecules were activated over the sample decorated with carbon species. In situ ESR spectra over C-BiOCl (Fig. 9b) further unveiled the trace of  $O_2$  reduction. To begin with, the ESR signals were attributed to the DMPO- $O_2^\bullet$  adduct. When the ultrasonic vibration was applied for about 180 s, the contribution of DMPO- $HO_2^\bullet$  adduct started to emerge. Quantitative analysis (Fig. 9c) revealed a total DMPO spin-adduct concentration of around  $110 \mu\text{M}$  was generated in the test, from which DMPO- $O_2^\bullet$  was predominant within the first 280 s and DMPO- $HO_2^\bullet$  took the lead in the remaining time. These results demonstrated the effective piezocatalytic  $O_2$  reduction into  $H_2O_2$  over C-BiOCl.

Based on the performance and characterizations, it was interesting to find that although carbon modification weakened the piezoresponse of BiOCl under the application of external stress, piezocatalytic  $H_2O_2$  production over C-BiOCl was facilitated. A rational conjecture was proposed as follows (Scheme 1). The decoration of carbon species not only raised the carrier density within BiOCl nanosheets but also served as active sites mediating the  $O_2$  adsorption and the subsequent electron injection. The resultant improvement in the  $H_2O_2$  production efficiency compensated for the negative impact on the attenuated piezoelectricity, which brought about an enhancement in the piezocatalytic activity. Namely, the regulation of the surface active sites for the specific target reaction might be a promising strategy to boost the piezocatalytic performance. As the final step of piezocatalysis, surface reaction directly determined the efficiency of mechanical-to-chemical energy conversion. With these inspirations in mind, the correlation between piezoresponse and surface reaction could be “manipulated”: (1) Screening highly active motifs for the target reaction; (2) Screening potential piezoelectrics that were expected to provide sufficient driving force; (3) Assembling the building blocks properly through surface engineering; and (4) Orthogonal evaluation for an optimized piezocatalytic performance. In a deeper sense, refinements and modular design towards piezoresponse, kinetics of the induced charges, and surface catalysis would be the future of piezocatalysis.

#### 4. Conclusion

In summary, piezocatalytic  $H_2O_2$  production was achieved over carbon-modified BiOCl nanosheets. In-depth analyses uncovered the

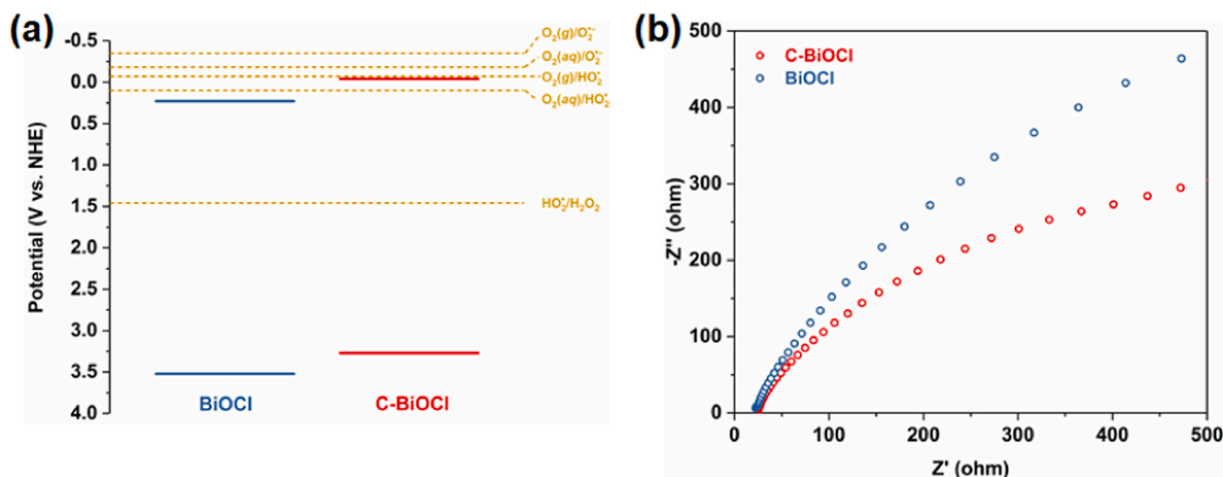


Fig. 7. Band structure alignments (a) and EIS spectra (b) of BiOCl and C-BiOCl.



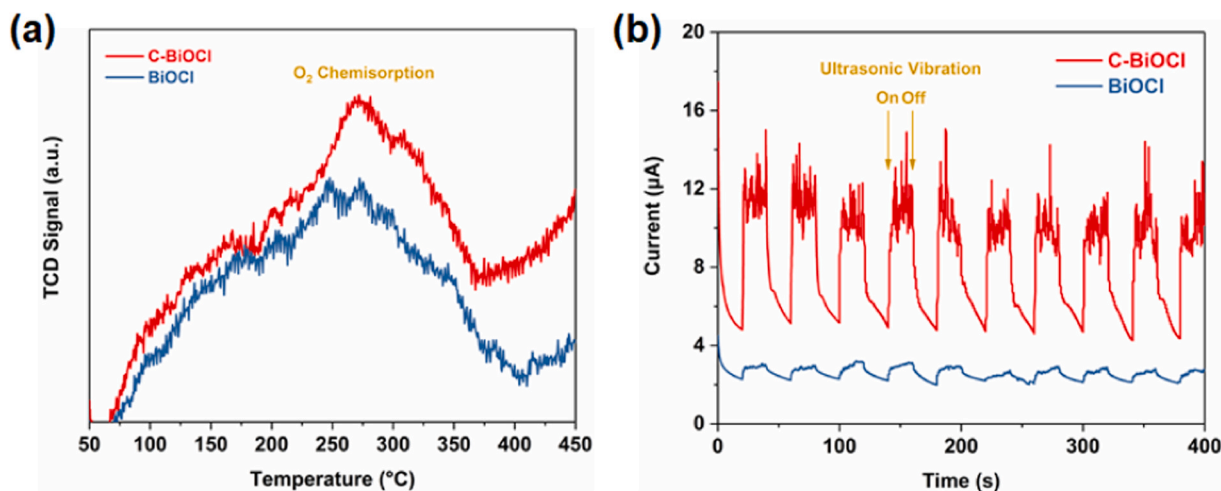


Fig. 8. (a)  $O_2$ -TPD spectra of BiOCl and C-BiOCl; (b) Transient current response of BiOCl and C-BiOCl under ultrasonic vibration.

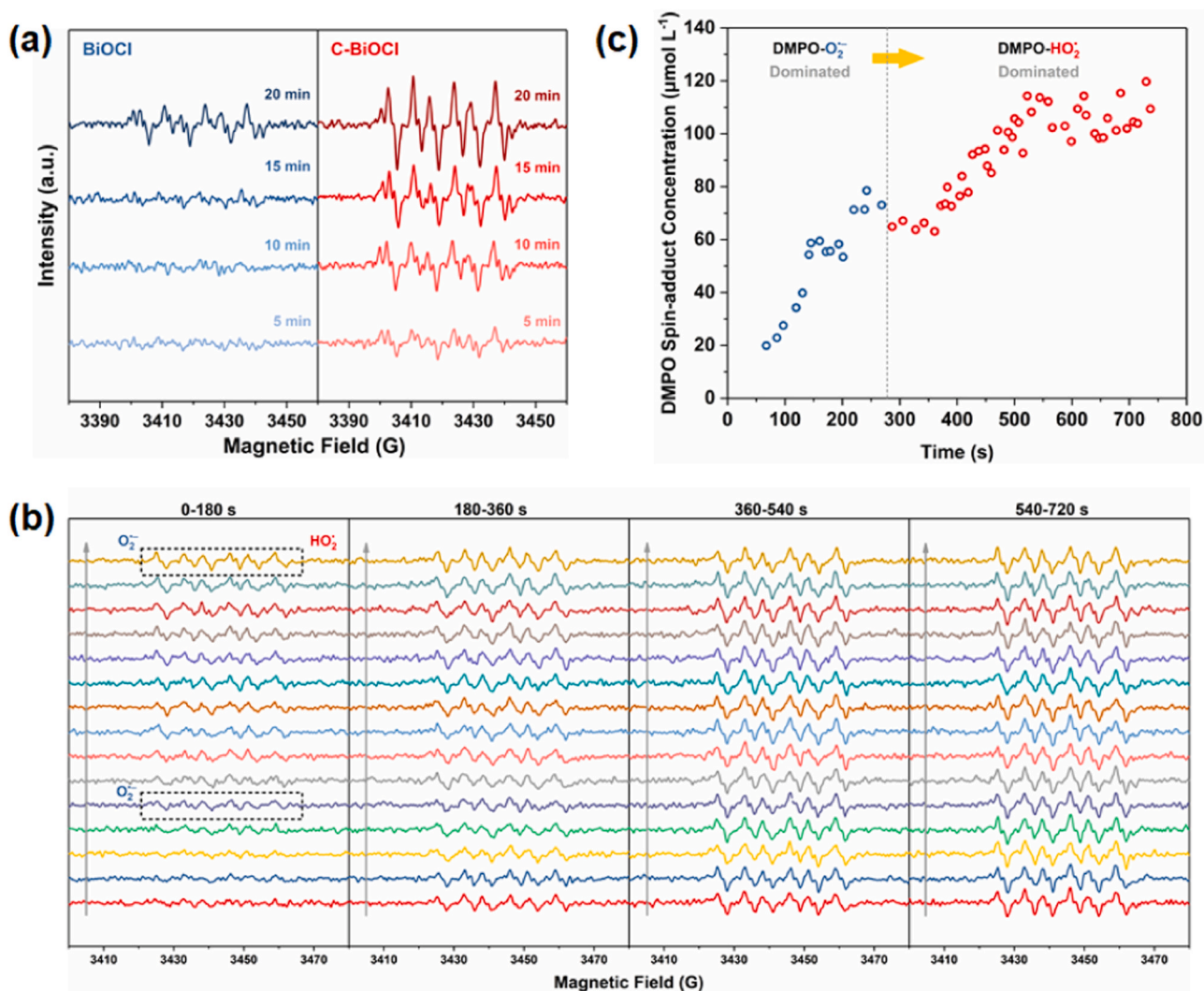
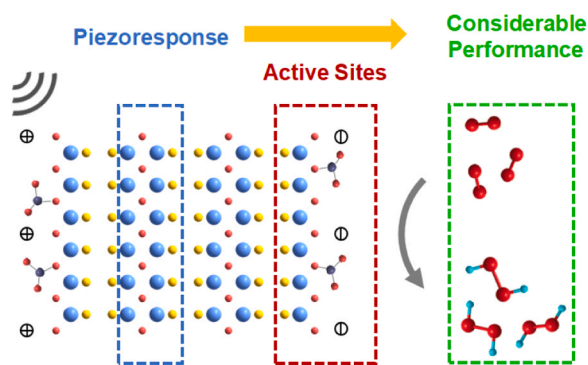


Fig. 9. (a) ESR spectra of the DMPO adduct generated by BiOCl and C-BiOCl; (b, c) In situ ESR spectra and quantitative analysis of the DMPO adduct over C-BiOCl.

correlation between piezoresponse and surface reaction. For the physical properties, carbon modification weakened the piezoelectricity of BiOCl, regulated the band structure alignments, and raised the carrier density. As to the surface reaction, the decoration of carbon species

served as the surface active sites that promoted  $O_2$  activation. The improvement of surface reaction compensated for the impact on piezoelectricity decline, and therefore the catalytic efficiency over C-BiOCl surpassed the pristine BiOCl. This work supplied a potential





Scheme 1. Piezocatalytic  $\text{H}_2\text{O}_2$  production over BiOCl catalysts.

scheme for the design of piezocatalytic systems.

## Funding

This work was supported by the National Natural Science Foundation of China (52202240, 82270756, 82000686); the China Postdoctoral Science Foundation (2021M701409); the Natural Science Foundation of Guangdong, China (2018A030313527); the Basic and Applied Basic Research Foundation of Guangdong Province, China (2019A1515010176); the Science and Technology Project of Guangzhou, China (202102010133); the Science and Technology Project of Shenzhen, China (JCYJ20190808095615389); the Science and Technology Project of Heyuan, China (Social Development and Rural Science No. 2023006, 2023009, 2023010); and the project of national local joint engineering laboratory to functional adsorption material technology for the environmental protection, Soochow University (No. SDGC2210).

## CRediT authorship contribution statement

**Yuanyi Zhou:** Conceptualization, Methodology, Formal analysis, Writing-original draft. **Haojie Dong:** Methodology, Formal analysis, Writing-original draft. **Zhaofen Xu:** Methodology. **Qingbing Zha:** Methodology. **Mingshan Zhu:** Conceptualization, Writing-review and editing, Supervision, Project administration. **Yu Meng:** Conceptualization, Methodology, Writing-review and editing, Supervision, Project administration.

## Declaration of Competing Interest

The authors declare that they have no known competing financial interests or personal relationships that could have appeared to influence the work reported in this paper.

## Data Availability

Data will be made available on request.

## Appendix A. Supporting information

Supplementary data associated with this article can be found in the online version at [doi:10.1016/j.apcatb.2023.123504](https://doi.org/10.1016/j.apcatb.2023.123504).

## References

- Q. Wu, J. Cao, X. Wang, Y. Liu, Y. Zhao, H. Wang, Y. Liu, H. Huang, F. Liao, M. Shao, A metal-free photocatalyst for highly efficient hydrogen peroxide photoproduction in real seawater, *Nat. Commun.* 12 (2021), 483, <https://doi.org/10.1038/s41467-020-20823-8>.
- S. Siahrostami, A. Verdager-Casadevall, M. Karamad, D. Deiana, P. Malacrida, B. Wickman, M. Escudero-Escribano, E.A. Paoli, R. Frydendal, T.W. Hansen, Enabling direct  $\text{H}_2\text{O}_2$  production through rational electrocatalyst design, *Nat. Mater.* 12 (2013) 1137–1143, <https://doi.org/10.1038/nmat3795>.
- Y. Bu, Y. Wang, G.F. Han, Y. Zhao, X. Ge, F. Li, Z. Zhang, Q. Zhong, J.B. Baek, Carbon-based electrocatalysts for efficient hydrogen peroxide production, *Adv. Mater.* 33 (2021), 2103266, <https://doi.org/10.1002/adma.202103266>.
- M.B. Starr, J. Shi, X. Wang, Piezopotential-driven redox reactions at the surface of piezoelectric materials, *Angew. Chem. Int. Ed.* 124 (2012) 6064–6068, <https://doi.org/10.1002/anie.201201424>.
- M. Wang, B. Wang, F. Huang, Z. Lin, Enabling PIEZOpotential in PIEZOelectric semiconductors for enhanced catalytic activities, *Angew. Chem. Int. Ed.* 58 (2019) 7526–7536, <https://doi.org/10.1002/anie.201811709>.
- M.B. Starr, X. Wang, Coupling of piezoelectric effect with electrochemical processes, *Nano Energy* 14 (2015) 296–311, <https://doi.org/10.1016/j.nanoen.2015.01.035>.
- M. Zhang, W. Guo, Y. Chen, D. He, A.B. Isaev, M. Zhu, Dissolved oxygen in aeration-driven piezo-catalytic for antibiotics pollutants removal in water, *Chin. Chem. Lett.* (2023), 108229, <https://doi.org/10.1016/j.ccl.2023.108229>.
- C. Yu, J. He, S. Lan, W. Guo, M. Zhu, Enhanced utilization efficiency of peroxymonosulfate via water vortex-driven piezo-activation for removing organic contaminants from water, *Environ. Sci. Ecotech.* 10 (2022), 100165, <https://doi.org/10.1016/j.ese.2022.100165>.
- J. He, Z. Yi, Q. Chen, Z. Li, J. Hu, M. Zhu, Harvesting mechanical energy induces piezoelectric polarization of MIL-100(Fe) for cocatalyst-free hydrogen production, *Chem. Commun.* 58 (2022) 10723–10726, <https://doi.org/10.1039/d2cc03976a>.
- W. Qian, W. Yang, Y. Zhang, C.R. Bowen, Y. Yang, Piezoelectric materials for controlling electro-chemical processes, *Nano-Micro Lett.* 12 (1) (2020) 39, <https://doi.org/10.1007/s40820-020-00489-z>.
- Y.C. Wang, J.M. Wu, Effect of controlled oxygen vacancy on  $\text{H}_2$ -production through the piezocatalysis and piezophotonics of ferroelectric R3C  $\text{ZnSnO}_3$  nanowires, *Adv. Funct. Mater.* 30 (2020), 1907619, <https://doi.org/10.1002/adfm.201907619>.
- S. Lan, C. Yu, E. Wu, M. Zhu, D.D. Dionysiou, Self-powered water flow-triggered piezocatalytic generation of reactive oxygen species for water purification in simulated water drainage, *ACS EST Engg* 2 (2021) 101–109, <https://doi.org/10.1021/acsestengg.1c00296>.
- Z. Ren, F. Chen, Q. Zhao, G. Zhao, H. Li, W. Sun, H. Huang, T. Ma, Efficient  $\text{CO}_2$  reduction to reveal the piezocatalytic mechanism: from displacement current to active sites, *Appl. Catal. B: Environ.* 320 (2023), 122007, <https://doi.org/10.1016/j.apcatb.2022.122007>.
- C. Zhai, Y. Chen, X. Huang, A.B. Isaev, M. Zhu, Recent progress on single-atom catalysts in advanced oxidation processes for water treatment, *Environ. Funct. Mater.* 1 (2022) 219–229, <https://doi.org/10.1016/j.efmat.2022.11.001>.
- A. Karunakaran, K.J. Francis, C.R. Bowen, R.J. Ball, Y. Zhao, L. Wang, N. B. McKeown, M. Carta, P.J. Fletcher, R. Castaing, Nanophase-photocatalysis: loading, storing, and release of  $\text{H}_2\text{O}_2$  using graphitic carbon nitride, *Chem. Commun.* 59 (2023) 7423–7426, <https://doi.org/10.1039/D3CC01442H>.
- Q. Zhao, H. Xiao, G. Huangfu, Z. Zheng, J. Wang, F. Wang, Y. Guo, Highly-efficient piezocatalytic performance of nanocrystalline  $\text{BaTiO}_{3-89}\text{SnO}_{11}$  catalyst with  $T_c$  near room temperature, *Nano Energy* 85 (2021), 106028, <https://doi.org/10.1016/j.nanoen.2021.106028>.
- J. Ai, C. Jin, D. Liu, J. Zhang, I. Zhang, Strain engineering to boost piezocatalytic activity of  $\text{BaTiO}_3$ , *e202201316*, *ChemCatChem* 15 (2023), <https://doi.org/10.1002/cctc.202201316>.
- S. Verma, M. Sharma, A. Halder, R. Vaish, Effect of poling on piezocatalytic and electrochemical properties of  $\text{Pb}(\text{Zr}_{0.52}\text{Ti}_{0.48})\text{O}_3$  ceramics, *Surf. Interfaces* 30 (2022), 101827, <https://doi.org/10.1016/j.surf.2022.101827>.
- R. Su, H.A. Hsain, M. Wu, D. Zhang, X. Hu, Z. Wang, X. Wang, F. Li, X. Chen, L. Zhu, Nano-ferroelectric for high efficiency overall water splitting under ultrasonic vibration, *Angew. Chem. Int. Ed.* 58 (2019) 15076–15081, <https://doi.org/10.1002/anie.201907695>.
- C. Yu, S. Lan, S. Cheng, L. Zeng, M. Zhu, Ba substituted  $\text{SrTiO}_3$  induced lattice deformation for enhanced piezocatalytic removal of carbamazepine from water, *J. Hazard. Mater.* 424 (2022), 127440, <https://doi.org/10.1016/j.jhazmat.2021.127440>.
- Y.P. Zhu, C. Guo, Y. Zheng, S.-Z. Qiao, Surface and interface engineering of noble-metal-free electrocatalysts for efficient energy conversion processes, *Acc. Chem. Res.* 50 (2017) 915–923, <https://doi.org/10.1016/j.ccr.2020.213374>.
- Y. Zheng, Z. Yu, H. Ou, A.M. Asiri, Y. Chen, X. Wang, Black phosphorus and polymeric carbon nitride heterostructure for photoinduced molecular oxygen activation, *Adv. Funct. Mater.* 28 (2018), 1705407, <https://doi.org/10.1002/adfm.201705407>.
- D. Shao, L. Zhang, S. Sun, W. Wang, Oxygen reduction reaction for generating  $\text{H}_2\text{O}_2$  through a piezo-catalytic process over bismuth oxychloride, *ChemSusChem* 11 (2018) 527–531, <https://doi.org/10.1002/cssc.201702405>.
- J. Yoon, J. Kim, F. Tieves, W. Zhang, M. Alcalde, F. Hollmann, C.B. Park, Piezobiocatalysis: ultrasound-driven enzymatic oxyfunctionalization of C–H bonds, *ACS Catal.* 10 (2020) 5236–5242, <https://doi.org/10.1021/acscatal.0c00188>.
- J. Luo, C. Feng, C. Fan, L. Tang, Y. Liu, Z. Gong, T. Wu, X. Zhen, H. Feng, M. Yan, Enhanced indirect attack behavior of  $^1\text{O}_2$  for photocatalytic  $\text{H}_2\text{O}_2$  production: possible synergistic regulation of spin polarization and water bridge on photocatalytic reaction, *J. Catal.* 413 (2022) 1132–1145, <https://doi.org/10.1016/j.jcat.2022.08.019>.
- Y. Long, H. Xu, J. He, C. Li, M. Zhu, Piezoelectric polarization of BiOCl via capturing mechanical energy for catalytic  $\text{H}_2$  evolution, *Surf. Interfaces* 31 (2022), 102056, <https://doi.org/10.1016/j.surf.2022.102056>.
- K. Fan, C. Yu, S. Cheng, S. Lan, M. Zhu, Metallic Bi self-deposited BiOCl promoted piezocatalytic removal of carbamazepine, *Surf. Interfaces* 26 (2021), 101335, <https://doi.org/10.1016/j.surf.2021.101335>.

- [28] Z. Lu, G. Chen, S. Siahrostami, Z. Chen, K. Liu, J. Xie, L. Liao, T. Wu, D. Lin, Y. Liu, High-efficiency oxygen reduction to hydrogen peroxide catalysed by oxidized carbon materials, *Nat. Catal.* 1 (2018) 156–162, <https://doi.org/10.1038/s41929-017-0017-x>.
- [29] S. Chen, T. Luo, K. Chen, Y. Lin, J. Fu, K. Liu, C. Cai, Q. Wang, H. Li, X. Li, Chemical identification of catalytically active sites on oxygen-doped carbon nanosheet to decipher the high activity for electro-synthesis hydrogen peroxide, *Angew. Chem. Int. Ed.* 133 (2021) 16743–16750, <https://doi.org/10.1002/anie.202104480>.
- [30] F. Sun, C. Yang, Z. Qu, W. Zhou, Y. Ding, J. Gao, G. Zhao, D. Xing, Y. Lu, Inexpensive activated coke electrocatalyst for high-efficiency hydrogen peroxide production: coupling effects of amorphous carbon cluster and oxygen dopant, *Appl. Catal. B: Environ.* 286 (2021), 119860, <https://doi.org/10.1016/j.apcatb.2020.119860>.
- [31] K. Gelderman, L. Lee, S. Donne, Flat-band potential of a semiconductor: using the Mott–Schottky equation, *J. Chem. Educ.* 84 (2007) 685, <https://doi.org/10.1021/ed084p685>.
- [32] T. Unuma, T. Sasaki, K. Yamaki, A. Irie, H. Ishida, T. Kato, Dielectric properties of crystalline BiOCl in the terahertz region, *OSA Contin.* 3 (2020) 2646–2652, <https://doi.org/10.1364/osac.399616>.
- [33] R. Al-Gaashani, A. Najjar, Y. Zakaria, S. Mansour, M. Atieh, XPS and structural studies of high quality graphene oxide and reduced graphene oxide prepared by different chemical oxidation methods, *Ceram. Int.* 45 (2019) 14439–14448, <https://doi.org/10.1016/j.ceramint.2019.04.165>.
- [34] Y. Qu, L. Wang, Z. Li, P. Li, Q. Zhang, Y. Lin, F. Zhou, H. Wang, Z. Yang, Y. Hu, Ambient synthesis of single-atom catalysts from bulk metal via trapping of atoms by surface dangling bonds, *Adv. Mater.* 31 (2019) 1904496, <https://doi.org/10.1002/adma.201970316>.
- [35] L. Zeng, F. Zhe, Y. Wang, Q. Zhang, X. Zhao, X. Hu, Y. Wu, Y. He, Preparation of interstitial carbon doped BiOI for enhanced performance in photocatalytic nitrogen fixation and methyl orange degradation, *J. Colloid Interface Sci.* 539 (2019) 563–574, <https://doi.org/10.1016/j.jcis.2018.12.101>.
- [36] X. Wang, H. Jiang, M. Zhu, X. Shi, Cascaded electron transition proved by femto-second transient absorption spectroscopy for enhanced photocatalysis hydrogen generation, *Chin. Chem. Lett.* 34 (2023), 107683, <https://doi.org/10.1016/j.cclet.2022.07.026>.
- [37] J. He, X. Wang, S. Jin, Z.-Q. Liu, M. Zhu, 2D metal-free heterostructure of covalent triazine framework/g-C<sub>3</sub>N<sub>4</sub> for enhanced photocatalytic CO<sub>2</sub> reduction with high selectivity, *Chin. J. Catal.* 43 (2022) 1306–1315, [https://doi.org/10.1016/s1872-2067\(21\)63936-0](https://doi.org/10.1016/s1872-2067(21)63936-0).
- [38] J. Sun, S. Wu, S.-Z. Yang, Q. Li, J. Xiong, Z. Yang, L. Gu, X. Zhang, L. Sun, Enhanced photocatalytic activity induced by sp<sup>3</sup> to sp<sup>2</sup> transition of carbon dopants in BiOCl crystals, *Appl. Catal. B: Environ.* 221 (2018) 467–472, <https://doi.org/10.1016/j.apcatb.2017.09.037>.
- [39] H. Huang, X. Li, J. Wang, F. Dong, P.K. Chu, T. Zhang, Y. Zhang, Anionic group self-doping as a promising strategy: band-gap engineering and multi-functional applications of high-performance CO<sub>3</sub><sup>2-</sup>-doped Bi<sub>2</sub>O<sub>2</sub>CO<sub>3</sub>, *ACS Catal.* 5 (2015) 4094–4103, <https://doi.org/10.1021/acscatal.5b00444>.
- [40] F. Dong, Y. Sun, M. Fu, W.-K. Ho, S.C. Lee, Z. Wu, Novel in situ N-doped (BiO)<sub>2</sub>CO<sub>3</sub> hierarchical microspheres self-assembled by nanosheets as efficient and durable visible light driven photocatalyst, *Langmuir* 28 (2012) 766–773, <https://doi.org/10.1021/la202752q>.
- [41] Y. Wang, X. Wen, Y. Jia, M. Huang, F. Wang, X. Zhang, Y. Bai, G. Yuan, Y. Wang, Piezo-catalysis for nondestructive tooth whitening, *Nat. Commun.* 11 (2020), 1328, <https://doi.org/10.1038/s41467-020-15015-3>.
- [42] M. Banoo, R.S. Roy, M. Bhakar, J. Kaur, A. Jaiswal, G. Sheet, U.K. Gautam, Bi<sub>4</sub>TaO<sub>8</sub>Cl as a new class of layered perovskite oxyhalide materials for piezopotential driven efficient seawater splitting, *Nano Lett.* 22 (2022) 8867–8874, <https://doi.org/10.1021/acs.nanolett.2c02900>.
- [43] D. Tiwari, S. Dunn, Influence of annealing on the photochemical deposition of silver onto PZT thin films under UV irradiation, *J. Eur. Ceram. Soc.* 29 (2009) 2799–2805, <https://doi.org/10.1016/j.jeurceramsoc.2009.03.018>.
- [44] P.M. Jones, S. Dunn, Interaction of Stern layer and domain structure on photochemistry of lead-zirconate-titanate, *J. Phys. D: Appl. Phys.* 42 (2009), 065408, <https://doi.org/10.1088/0022-3727/42/6/065408>.
- [45] A.-Y. Zha, Q.-B. Zha, Z. Li, H.-M. Zhang, X.-F. Ma, W. Xie, M.-S. Zhu, Surfactant-enhanced electrochemical detection of bisphenol A based on Au on ZnO/reduced graphene oxide sensor, *Rare Met.* 42 (2023) 1274–1282, <https://doi.org/10.1007/s12598-022-02172-1>.